Applied Physics B (2024) 130:71
https://doi.org/10.1007/s00340-024-08203-2

Applied Physics B
Lasers and Optics

RESEARCH

Collisional shifts of hyperfine resonances of ground-state atoms calculated with modified pseudopotential and orthogonalization

Kiyoshi Ishikawa[1]

Received: 8 January 2024 / Accepted: 7 March 2024 / Published online: 10 April 2024

Abstract
Hyperfine splitting frequency shifts of paramagnetic atoms (H, Li, Na, K, Rb, and Cs) induced by noble-gas collisions are calculated by perturbation theory. The finite sizes of the core orbitals of noble-gas atoms (He, Ne, Ar, Kr, and Xe) are taken into account by the modified pseudopotential. The wave function of the valence electron is orthogonalized to the core orbitals, leading to a correct calculation of the resonance frequency. Fitting results are compared for the wave function bases and the core orbital sizes. The best fits are obtained when the Hartree–Fock–Roothaan wave function is used for the ground state of paramagnetic atoms and when repulsion forces due to the outermost occupied orbitals of noble-gas atoms are considered. For all combinations of alkali-metal and noble-gas atoms, the obtained fitting parameters are close to the pseudopotential height of approximately 2.6 times the atomic radius.

1 Introduction

The hyperfine splitting frequency of the ground state of alkali-metal atoms has been studied intensively both experimentally and theoretically [1–7]. Frequency shifts were measured in buffer gases but have not been well explained by simple theories based on atomic orbitals. A negative frequency shift was obtained with dispersion potentials for heavier noble-gas atoms. However, as the atoms became heavier, the measured frequency shifts and their temperature dependence could not be satisfactorily explained. Recently, the introduction of turning points in collisions has made it possible to numerically reproduce frequency shifts over a wide temperature range, from light to heavy noble-gas atoms [8]. Despite various improvements, however, some of the obtained parameters do not provide physical insight.

The Fermi pseudopotential has been used for *s*-wave scattering and can also describe the repulsion force in atomic collisions at room temperature or above. The pseudopotential is a good approximation for collision partners with small atomic radii. In collisions with heavier *noble-gas* atoms, the radii of the occupied core orbitals should be considered in the repulsion force. Therefore, the pseudopotential is modified to take into account the overlap of the wave functions of the valence electron and the electrons in core orbitals. On the other hand, the theoretical repulsion potential had been systematically obtained based on the Coulomb-approximation (CA) wave function [9]. Therefore, the theoretical potential curve and the CA wave function were used to calculate the frequency shift [7, 8]. However, for heavier *alkali-metal* atoms, the CA wave function deviates significantly from more accurate functions such as the Hartree–Fock–Roothaan (HFR) wave function [10, 11]. In calculations, the fitting parameters might have presented systematic bias due to the alkali-metal dependence, which is inevitably included in the theoretical potentials. This work compares calculations using the CA and the HFR wave functions to check if this bias happened.

The perturbed wave functions of the valence electrons are orthogonalized to the core orbitals of the noble-gas atoms. The orthogonalization changes the electron density, that is, the magnitude of spin interaction at the positions of both nuclei of collision pairs. The orthogonalized wave approximation (OWA) has explained the enhanced spin-exchange interaction between valence electrons and noble-gas nuclei [12, 13], which is a key interaction in modern quantum devices of ensemble atomic vapor [14, 15]. In addition to this enhancement, the numerical calculations in this work provide details of the frequency shift of hyperfine resonance, i.e., the change in the magnitude of the interaction between valence electrons and nuclei of the paramagnetic atoms.

✉ Kiyoshi Ishikawa
ishikawa@sci.u-hyogo.ac.jp

[1] Graduate School of Science, University of Hyogo, Hyogo 678-1297, Japan

In the text, paramagnetic atoms such as hydrogen and the alkali-metal atom are referred to as atom a, and noble-gas atoms as atom b.

2 Hyperfine splitting frequency

2.1 Isotropic interaction

The isotropic hyperfine interaction in the ground state is expressed by the scalar magnetic dipole coupling, $A\boldsymbol{I}\cdot\boldsymbol{S}$, where $\boldsymbol{I}$ is the nuclear spin and $\boldsymbol{S}$ is the electron spin of an atom a [16]. The hyperfine constant A is proportional to the density of the valence electron at the position of nucleus a. When mean density changes by atomic collisions, the hyperfine constant also changes, $A = A_g + \delta A_g$, where A_g is the hyperfine constant of a free atom in the vacuum.

2.2 Analysis results

The hyperfine splitting frequencies in noble gases, $\nu = \nu_0 + \delta\nu$, are analyzed in terms of an isotope-independent dimensionless parameter λ [4, 17],

$$\lambda = \frac{1}{Na_0^3}\frac{\delta\nu}{\nu_0} = \frac{1}{Na_0^3}\frac{\delta A_g}{A_g}, \tag{1}$$

where $\nu_0 = A_g(2I+1)/2h$ is the unperturbed frequency measured in vacuum, $\delta\nu$ is the measured frequency shift, N is the number density of noble-gas atoms, a_0 is the Bohr radius, and h is the Planck constant. The measurements used in this work were performed in dilute noble gases. Therefore, we assume $\delta\nu \propto N$ due to binary collisions and ignore nonlinear shifts due to many-body collisions and the formation of van der Waals molecules [18, 19]. The relative shift λ obtained from the measured $\delta\nu$ is compared with λ from the theoretical δA_g. The shifts λ depend on the temperature for the respective collision pairs. Figure 1 shows previously measured shifts and the fitting curves calculated in this work. The theory and analysis conditions are described in the following sections. The frequency shifts have been measured over a wide temperature range in He, Ne, and Ar gases. Therefore, the fitting curves are reliably obtained. In Kr and Xe gases, however, the small number of measured shifts may have caused ambiguity in the fitting. For Rb and Cs atoms, if ξ in Eq. (21) is greater than the current value in Table 2, the difference between the calculated shifts for each condition is reduced, although it cannot be judged based on the measurements to date.

2.3 Collision processes

The frequency shift is obtained by assuming that binary collisions are weak and sudden. The phase of hyperfine coherence changes continuously and incoherent interruptions are neglected. The phase angle ϕ added in a single collision is sufficiently small and assumed to be proportional to $\delta A_g(t)$. The frequency shift becomes nonlinear as ϕ increases. It takes place by the formation of van der Waals molecules [18, 19]. At the high-temperature approximation, we ignore the bound states in the potentials, such as vibrational and rotational states of molecules, and the spin interactions between atoms a and b [20, 21]. Except for the duration of collisions, the interaction energy $L(t) = \delta A_g(t)\boldsymbol{I}\cdot\boldsymbol{S}$ is negligible. With a large number of collisions, the atomic density operator ρ follows [22],

$$\begin{aligned}\frac{\partial\rho}{\partial t} =& -\frac{i}{\hbar}[H_\mathrm{a},\rho] \\ &-\frac{i}{\hbar T_\mathrm{c}}\left\langle[\check{L}(0),\rho]\right\rangle + \frac{1}{2\hbar^2 T_\mathrm{c}}\left\langle\left[\check{L}(0),[\check{L}(0),\rho]\right]\right\rangle,\end{aligned} \tag{2}$$

where H_a is the Hamiltonian of isolated atom a, T_c is mean time from one collision to the next, $\check{L}(\omega)$ is Fourier transform of $L(t)$, and $\check{L}^\dagger(0) = \check{L}(0)$. The first term shows the time evolution of isolated atoms, the second term is the frequency shift, and the third is the relaxation of hyperfine levels [4, 5]. The frequency is shifted by the interaction $L(t)$, but the linewidth may or may not broaden depending on the adiabatic potential. Other relaxation mechanisms, such as spin-rotation interactions, are dominant at high temperatures but are neglected because they do not cause frequency shifts [13, 22, 23]. Equation (2) is the same as the ensemble average of the quantum Lindblad master equations [24, 25]. Therefore, an atomic ensemble can be regarded as a single quantum system. Noting the frequency shift of the atomic system,

$$\delta\nu = \frac{\langle\phi\rangle}{2\pi T_\mathrm{c}}\frac{2I+1}{2}, \tag{3}$$

where the phase angle, $\phi = \frac{1}{\hbar}\int_{-\infty}^{\infty}\delta A_g(t)dt$, is an integral along a classical path [26]. The adiabatic potential in Sect. 3.2 changes the collision trajectory but not the internal spin state. The ensemble average in Eq. (3) is approximated by a statistical average in Sect. 3.4.2.

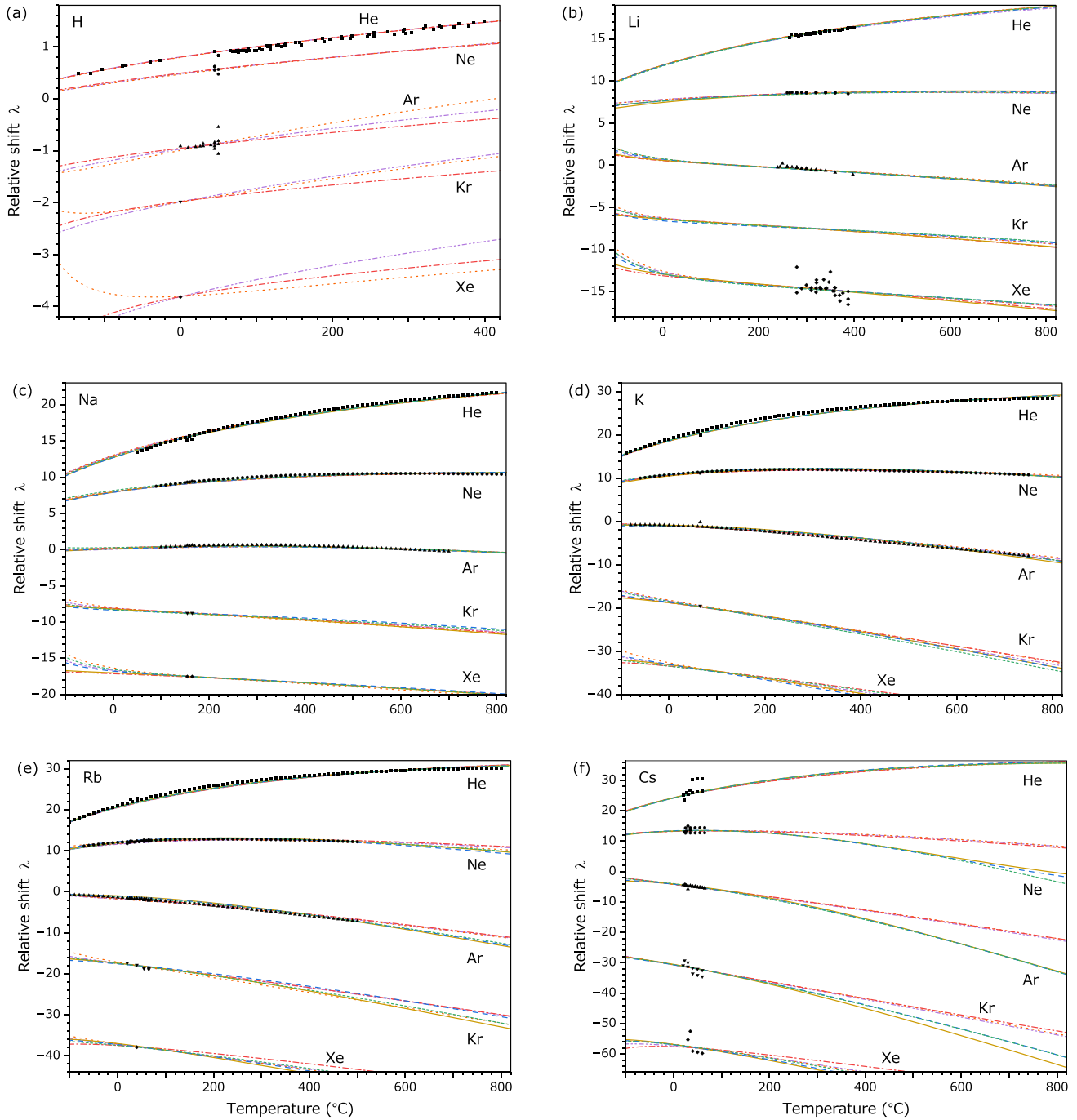

Fig. 1 Isotope-independent relative shift λ of **a** H [27–31], **b** Li [32, 33], **c** Na [17, 34, 35], **d** K [17, 35, 36], **e** Rb [17, 35, 37–45], and **f** Cs [37, 41, 45–50] atoms in noble gases. Marks indicate measured shifts. For Li in Kr and K in Xe, the shifts have not been measured and are estimated in calculations. Note that the temperature range for hydrogen is different from the others. Fitting curves are calculated using the Coulomb-approximation (CA) and the Hartree–Fock–Roothaan (HFR) wave functions. The electron density of noble-gas atoms is assumed to be the delta function (DLT), all core orbitals (ALC), and outermost core orbitals (OMT). The curves are brown solid (HFR, OMT), blue dashed (HFR, ALC), green short-dashed (HFR, DLT), red dashed-dotted (CA, OMT), purple dashed-dotted-dotted (CA, ALC), and orange dotted (CA, DLT). For hydrogen in Ar, Kr, and Xe, fitting curves show unreasonable temperature dependence by DLT

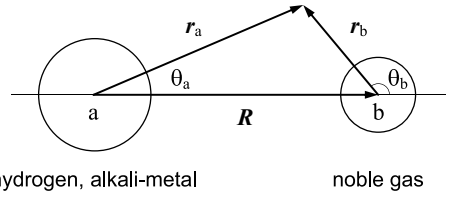

Fig. 2 Displacement vectors for $\boldsymbol{r}_a = \boldsymbol{r}_b + \boldsymbol{R}$. $\boldsymbol{r}_a$ and $\boldsymbol{R}$ are, respectively, the displacements of electrons and the nucleus b from the nucleus a. $\boldsymbol{r}_b$ is the displacement of electrons from the nucleus b

3 Perturbation theory

3.1 Wave function

The electron wave function is expressed by the direct product, $\phi_v(\boldsymbol{r}_a)\phi_c(\boldsymbol{r}_a)\phi_b(\boldsymbol{r}_b)$, where $\phi_v(\boldsymbol{r}_a)$ is the wave function of valence electron, $\phi_c(\boldsymbol{r}_a) = \prod_i \phi_{ci}(\boldsymbol{r}_{ai})$ of the occupied core orbitals of atom a, $\phi_b(\boldsymbol{r}_b) = \prod_i \phi_{bi}(\boldsymbol{r}_{bi})$ of the occupied core orbitals of atom b, $\boldsymbol{r}_a$ is a displacement of electron from nucleus a, and $\boldsymbol{r}_b$ is a displacement of electron from nucleus b. The displacement vectors are shown in Fig. 2. At a sufficiently far internuclear distance R, the valence electron is in the ground state of the atom a, $\phi_v(\boldsymbol{r}_a) = \phi_{ag}(\boldsymbol{r}_a)$. In atomic collisions, the valence electron is perturbed by atom b. The perturbed wave functions are obtained in Sect. 3.3.1. For core electrons, wave functions $\phi_{ci}(\boldsymbol{r}_{ci})$ are orthogonal to each other. The same holds for $\phi_{bi}(\boldsymbol{r}_{bi})$. In addition, these can be considered orthogonal to each other since the overlap of $\phi_{ci}(\boldsymbol{r}_{ci})$ with $\phi_{bi}(\boldsymbol{r}_{bi})$ is negligible even at the closest distance in atomic collisions, as shown in Sect. 3.2.1. The perturbed wave function $\phi_v(\boldsymbol{r}_a)$ is orthogonalized to the core orbitals, $\phi_{bi}(\boldsymbol{r}_{bi})$, in Sect. 3.3.2.

3.1.1 Hartree–Fock–Roothaan (HFR) wave function

The HFR wave function is used for the ground state of valence electrons and the core orbitals of atoms a and b [10, 11]. Non-relativistic wave functions do not represent electrons near the nucleus well. In particular, the amplitude $\phi_{ki}(0)$ of the s orbitals differs from the measured value, and the difference is wider for heavier atoms. For example, the ratios of calculated and measured densities $|\phi_{ag}(0)|^2$ are, respectively, 0.978 (H), 0.723 (Li), 0.706 (Na), 0.625 (K), 0.554 (Rb), and 0.428 (Cs). These differences are corrected for atoms a in the following calculations, but not for noble-gas atoms. The HFR wave function is a one-electron wave function based on the mean-field approximation. Since, for hydrogen atoms, there is only one electron, the HFR wave function is the same as the CA wave function.

3.1.2 Coulomb-approximation (CA) wave function

The CA wave function is used for the excited state of atom a. For comparison with the HFR wave function, the CA wave function is also used for the ground state of the valence electron. For hydrogen atoms, given the excitation energy, the CA wave function is identical to the analytic, non-relativistic form in the Coulomb potential [51]. Since the thermal energy is small compared to the repulsive potential, colliding atoms rarely get closer to each other to a distance where the CA wave function becomes inaccurate. Therefore, the CA wave function can be used outside the closest distance (classical turning point). In Refs. [7, 8], for the ground state, the CA wave function was needed to reproduce the theoretical repulsive potential based on the CA wave function [52]. The height in Eq. (7) was fixed to the theoretical potential. In this work, the potential height is treated as a fitting parameter. Therefore, the CA wave function is one of the options for best fitting the measured hyperfine frequency shift.

3.1.3 Spin-orbit coupling

For core electrons, the radial wave function $R_{bil}(r_b)$, which is common to individual shells, is used in the form given as the HFR basis function. Therefore, assuming uncoupled states, the wave function is the direct product of the radial, orbital, and spin basis functions, respectively,

$$\phi_{bi}(\boldsymbol{r}_b) = R_{bil}(r_b)Y_{lm_l}(\theta_b, \varphi_b)\chi_{m_s}(\sigma_b), \tag{4}$$

where $\boldsymbol{i}$ is a set of quantum numbers (i, l, m_l, m_S). The direct product is also assumed for the core electrons of atom a. For valence electrons with spin-orbit interaction, we take the linear combination of the direct product,

$$\phi_{a\boldsymbol{n}}(\boldsymbol{r}_a) = R_{anlj}(r_a) \sum_{m_l, m_S} C^{jm}_{lm_l\frac{1}{2}\sigma} Y_{lm_l}(\theta_a, \varphi_a)\chi_{m_s}(\sigma_a), \tag{5}$$

Table 1 The number of core electrons of noble gas N_e. The measured electric-dipole polarizability α [56, 57], s-wave electron scattering length a_s [58], and van der Waals radius R_{vdw} [56]. Atomic radius R_{sto} calculated by single Slater-type wave functions [59] and R_{hfr} by the HFR wave functions. These are in atomic units

	He	Ne	Ar	Kr	Xe
$N_e/2$	1	5	9	18	27
α	1.3873	2.6705	11.150	16.905	27.554
a_s	1.19	0.214	− 1.492	− 3.32	−6.0
R_{vdw}	2.51	2.25	2.79	2.99	3.26
R_{sto}	0.593	0.716	1.35	1.66	2.04
R_{hfr}	0.569	0.634	1.302	1.568	1.938

where $C^{jm}_{lm_l s\sigma}$ is a Clebsch-Gordan coefficient, $Y_{lm_l}(\theta, \varphi)$ is the spherical harmonic, and $\boldsymbol{n} = (n, l, j, m)$. The radial function $R_{anlj}(r_a)$ is given by the HFR or CA wave function.

3.2 Adiabatic potential

The total Hamiltonian is $H_a + H_b + H'$, where H_a and H_b are the Hamiltonians of isolated atoms, respectively. Fermi pseudopotential, $(2\pi\hbar^2 a_s/m_e)\delta(\boldsymbol{r}_a - \boldsymbol{R})$, has been used for the repulsive interaction between the valence electron of atom a and the electrons of atom b, where m_e is the electron mass [4]. The scattering length of slow electrons a_s characterizes the interaction. See Table 1. In the absence of dispersion potential, the scattering length corresponds to the radius of the hard-sphere model. We will use this relation in the following discussion. However, different from the Rydberg state [53–55], the orbitals of the ground-state valence electrons do not have the sufficient spatial extent to assume atomic collisions described only by s waves. If the radius of the occupied orbitals of atom b is smaller than the orbital radius of the valence electron, the interaction is approximately described by a Fermi pseudopotential. Otherwise, the size of atom b should be included in the calculation. This is truly the case for hydrogen atoms. In the case of alkali-metal atoms, the finite size of noble gas atoms causes small but meaningful changes in the fitting parameters.

3.2.1 Pseudopotential

For the finite size of the core orbital of atom b, we take the interaction Hamiltonian to be,

$$H'(\boldsymbol{r}_a, \boldsymbol{r}_b, \boldsymbol{R}) = 4\pi V_h \sum_i \delta(\boldsymbol{r}_a - \boldsymbol{r}_{bi} - \boldsymbol{R}), \tag{6}$$

where $\boldsymbol{r}_a$ is the displacement of valence electron, $\boldsymbol{r}_b$ is representative of all $\boldsymbol{r}_{bi}$, the sum takes over the occupied shells of atom b, and $V_h = \hbar^2 a_h/2m_e$. The potential height a_h depends on both the atoms, a and b. The expectation value of the interaction $\langle b|\langle a\boldsymbol{g}|H'|a\boldsymbol{g}\rangle|b\rangle$ is,

$$V_{\boldsymbol{g}}(R) = 4\pi V_h \int d^3\boldsymbol{r}_a |\phi_{a\boldsymbol{g}}(\boldsymbol{r}_a)|^2 \sum_i |\phi_{b\boldsymbol{i}}(\boldsymbol{r}_{bi})|^2, \tag{7}$$

where $\boldsymbol{r}_a = \boldsymbol{r}_{bi} + \boldsymbol{R}$ and $\rho_b(\boldsymbol{r}_b) = \sum_i |\phi_{b\boldsymbol{i}}(\boldsymbol{r}_{bi})|^2$ is the electron density distribution. $V_{\boldsymbol{g}}(R)$ presents the repulsive potential of atoms a and b. For the Fermi pseudopotential, $\rho_b(\boldsymbol{r}_b) = \delta(\boldsymbol{r}_b)$ and $V_{\boldsymbol{g}}(R) = 4\pi V_h |\phi_{a\boldsymbol{g}}(R)|^2$ in Eq. (7). Explicit forms for numerical calculation are given in Appendix A. The repulsion potential due to the core electrons of both atoms a and b is assumed as,

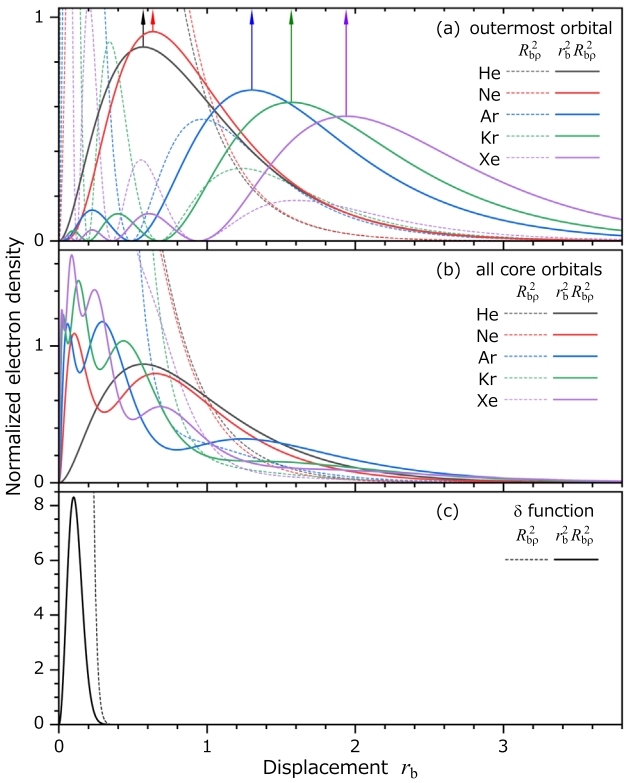

Fig. 3 Normalized electron-density distribution of noble-gas atoms. **a** the outermost orbital, **b** all occupied orbitals, and **c** the delta function approximated by $\rho(r_b) = (\sqrt{\pi}a)^{-3} \exp\left(-(r_b/a)^2\right)$, where $a = 0.1$. The vertical arrow in **a** indicates the radius R_{hfr} at which $r_b R_{b\rho}(r_b)$ is maximum

$$V_c(R) = 4\pi V_h \int d^3\boldsymbol{r}_a \sum_i |\phi_{c\boldsymbol{i}}(\boldsymbol{r}_{ai})|^2 \rho_b(\boldsymbol{r}_b). \tag{8}$$

The convolution between the core orbitals changes the fitting parameter a_h for the largest noble gas, Xe atoms, by at most 1 % compared to the case of $\rho_b(\boldsymbol{r}_b) = \delta(\boldsymbol{r}_b)$ in Eq. (8).

3.2.2 Electron density of noble-gas atoms

The calculation is performed for various normalized electron densities $\rho_b(\boldsymbol{r}_b)$, such as the delta function $\delta(\boldsymbol{r}_b)$ (called DLT), sum of all core orbitals $\sum_i |\phi_{b\boldsymbol{i}}(\boldsymbol{r}_{bi})|^2$ (ALC), and the outermost orbital $|\phi_{b\boldsymbol{i}}(\boldsymbol{r}_{bi})|^2$ (OMT), as shown in Fig. 3. Empirical atomic radii R_{sto} were obtained from the radius of maximum electron density, $r_b\phi_{b\boldsymbol{i}}(r_b)$, in the outermost shell using single Slater-type orbitals [59]. Similarly, the radii R_{hfr} are obtained for HFR wave functions, as shown in Table 1. The electron density of occupied orbitals of the noble-gas atoms is spherical symmetric by sum for azimuthal quantum number m_l.

Therefore, $\rho_{\rm b}(\boldsymbol{r}_{\rm b}) = (R_{{\rm b}\rho}(r_{\rm b})/\sqrt{4\pi})^2$ and normalized as $\int d^3\boldsymbol{r}_{\rm b}\, \rho_{\rm b}(\boldsymbol{r}_{\rm b}) = \int_0^\infty dr_{\rm b} \left(r_{\rm b} R_{{\rm b}\rho}(r_{\rm b})\right)^2 = 1$. As the outermost shell, we take 1*s* (He), 2*p* (Ne), 3*p* (Ar), 4*p* (Kr), and 5*p* orbitals (Xe). For the Ne atom, the radius of the maximum electron density of the 2*s* orbital (0.716) is greater than that of the 2*p* orbital (0.695). As the outermost orbital, however, we take the 2*p* orbitals that have wider feet than the 2*s* orbitals have because the convolution in Eq. (7) is more affected by the foot of orbitals.

3.2.3 Dispersion potential

For instantaneous molecules a–b, dispersion forces minimize the energy of the adiabatic potential. Previously calculated dispersion potential is expressed as [52, 60],

$$V_{\rm vdW}(R) = -f_6(R)\frac{C_6}{R^6} - f_8(R)\frac{C_8}{R^8}, \tag{9}$$

where $f_n(R)$ is the damping function changing from 1 to 0 as the colliding pair approaches. In Sect. 3.4, the adiabatic potential, $V(R) = V_{\rm c}(R) + V_{\boldsymbol{g}}(R) + V_{\rm vdW}(R)$, is used for the statistical average. The electrons are attracted to the induced dipole in the dispersion forces, and the electron density decreases at the nucleus a. This density decrease can be calculated by second-order perturbation theory [8]. In this work, the change in electron density is assumed to be proportional to the dispersion potential [1], as shown in Eq. (18), and the proportionality coefficient is obtained by fitting.

3.3 Linear combination of atomic orbitals (LCAO)

When electrons fill the orbitals of atoms a and b in sequence, each core orbital is occupied first, and the last electron enters the valence orbital. The valence electron is perturbed with the core electrons of atom b. The perturbed wave function $\phi_{\rm v}(\boldsymbol{r}_{\rm a})$ is represented by a linear combination of atomic orbitals (LCAO) and consists mainly of $\phi_{{\rm a}\boldsymbol{g}}(\boldsymbol{r}_{\rm a})$ with the mixing of the excited states $\phi_{{\rm a}\boldsymbol{n}}(\boldsymbol{r}_{\rm a})$ and $\phi_{{\rm b}\boldsymbol{n}}(\boldsymbol{r}_{\rm b})$ of atoms a and b, respectively. In general, $\phi_{\rm v}(\boldsymbol{r}_{\rm a}) = c_{{\rm a}\boldsymbol{g}\boldsymbol{g}}\phi_{{\rm a}\boldsymbol{g}}(\boldsymbol{r}_{\rm a}) + \sum_n c_{{\rm a}\boldsymbol{n}\boldsymbol{g}}\phi_{{\rm a}\boldsymbol{n}}(\boldsymbol{r}_{\rm a}) + \sum_n c_{{\rm b}\boldsymbol{n}\boldsymbol{g}}\phi_{{\rm b}\boldsymbol{n}}(\boldsymbol{r}_{\rm b})$. However, $\phi_{{\rm b}\boldsymbol{n}}(\boldsymbol{r}_{\rm b})$ in the last term corresponds to the negative ion states, where an electron enters the excited state outside the neutral closed shell of the noble-gas atom [61], which is scarcely induced by atomic collisions. Therefore, we ignore the last term.

3.3.1 Mixing of excited states of paramagnetic atom

Due to the interaction Hamiltonian H' in Eq. (6), the valence electron wave function is expressed in an LCAO form as,

$$\phi_{\rm v}(\boldsymbol{r}_{\rm a}, R) = \left\{1 + c_{\rm a2}(R)\right\}\phi_{{\rm a}\boldsymbol{g}}(\boldsymbol{r}_{\rm a}) + \sum_{\boldsymbol{n}>\boldsymbol{g}} c_{{\rm a}\boldsymbol{n}\boldsymbol{g}}(R)\phi_{{\rm a}\boldsymbol{n}}(\boldsymbol{r}_{\rm a}), \tag{10}$$

where the sum extends over all excited states. For normalization, $2c_{\rm a2} = -\sum c_{{\rm a}\boldsymbol{n}\boldsymbol{g}}^2 < 0$. The mixing coefficient $c_{{\rm a}\boldsymbol{n}\boldsymbol{g}}$ is obtained by perturbation theory as $-\langle {\rm b}|\langle {\rm a}\boldsymbol{n}|H'|{\rm a}\boldsymbol{g}\rangle|{\rm b}\rangle/E_{\boldsymbol{n}}$ and higher-order terms due to second-order perturbation theory are neglected. $E_{\boldsymbol{n}}$ is the excitation energy measured from the ground state and $E_{\boldsymbol{g}} = 0$ [62, 63]. Therefore,

$$c_{{\rm a}\boldsymbol{n}\boldsymbol{g}}(R) = -\frac{4\pi V_{\rm h}}{E_{\boldsymbol{n}}}\int d^3\boldsymbol{r}_{\rm a}\phi_{{\rm a}\boldsymbol{n}}^*(\boldsymbol{r}_{\rm a})\phi_{{\rm a}\boldsymbol{g}}(\boldsymbol{r}_{\rm a})\rho_{\rm b}(\boldsymbol{r}_{\rm b}). \tag{11}$$

The mixing leads to the change in electron density at nucleus a and the decrease in electron density at nucleus b. It means that, due to the pseudopotential, the occupied shells repel the valence electron at the position of nucleus b and induce the frequency shifts of hyperfine resonances of the atom a. The change in electron density due to the higher-order terms is equivalently included in change due to dispersion forces in Eq. (18) [8]. For the Fermi pseudopotential, $c_{{\rm a}\boldsymbol{n}\boldsymbol{g}}(R) = -(4\pi V_{\rm h}/E_n)\phi_{{\rm a}\boldsymbol{n}}(R)\phi_{{\rm a}\boldsymbol{g}}(R)$. Explicit forms for numerical calculation are given in Appendix B.

3.3.2 Orthogonalized wave approximation (OWA)

The wave function of valence electrons should be orthogonal to all other wave functions. Since $\phi_{\rm v}(\boldsymbol{r}_{\rm a}, R)$ in Eq. (10) is intrinsically orthogonal to all occupied shells of the atom a, it will be orthogonalized to all occupied shells of the atom b [13]. The OWA best approximates the wave function inside the core of the noble gas and reproduces atomic collisions along with further perturbations due to the pseudopotential [12]. The OWA wave function of valence electron is,

$$\psi(\boldsymbol{r}_{\rm a}, R) = \left\{1 + c_{\rm o2}(R)\right\}\phi_{\rm v}(\boldsymbol{r}_{\rm a}) - \sum_{\boldsymbol{i}\le\boldsymbol{g}} c_{{\rm o}\boldsymbol{i}}(R)\phi_{{\rm b}\boldsymbol{i}}(\boldsymbol{r}_{\rm b}), \tag{12}$$

where $2c_{\rm o2} = \sum c_{{\rm o}\boldsymbol{i}}^2$ for normalization and $c_{\rm o2} > 0$ since $\phi_{{\rm a}\boldsymbol{n}}(\boldsymbol{r}_{\rm a})$ is not orthogonal to $\phi_{{\rm b}\boldsymbol{i}}(\boldsymbol{r}_{\rm b})$. Therefore, the electron density at the nucleus a is increased by OWA. The orthogonalization coefficient $\langle {\rm b}\boldsymbol{i}|{\rm v}\rangle$ is

$$c_{{\rm o}\boldsymbol{i}}(R) = \sum_{\boldsymbol{n}\ge\boldsymbol{g}} c_{{\rm a}\boldsymbol{n}\boldsymbol{g}}(R)\int d^3\boldsymbol{r}_{\rm b}\, \phi_{{\rm b}\boldsymbol{i}}^*(\boldsymbol{r}_{\rm b})\phi_{{\rm a}\boldsymbol{n}}(\boldsymbol{r}_{\rm a}), \tag{13}$$

where $c_{{\rm a}\boldsymbol{g}\boldsymbol{g}} = 1 + c_{\rm a2}$. The OWA increases the number of nodes in the wave function and thus the eigenenergy. The

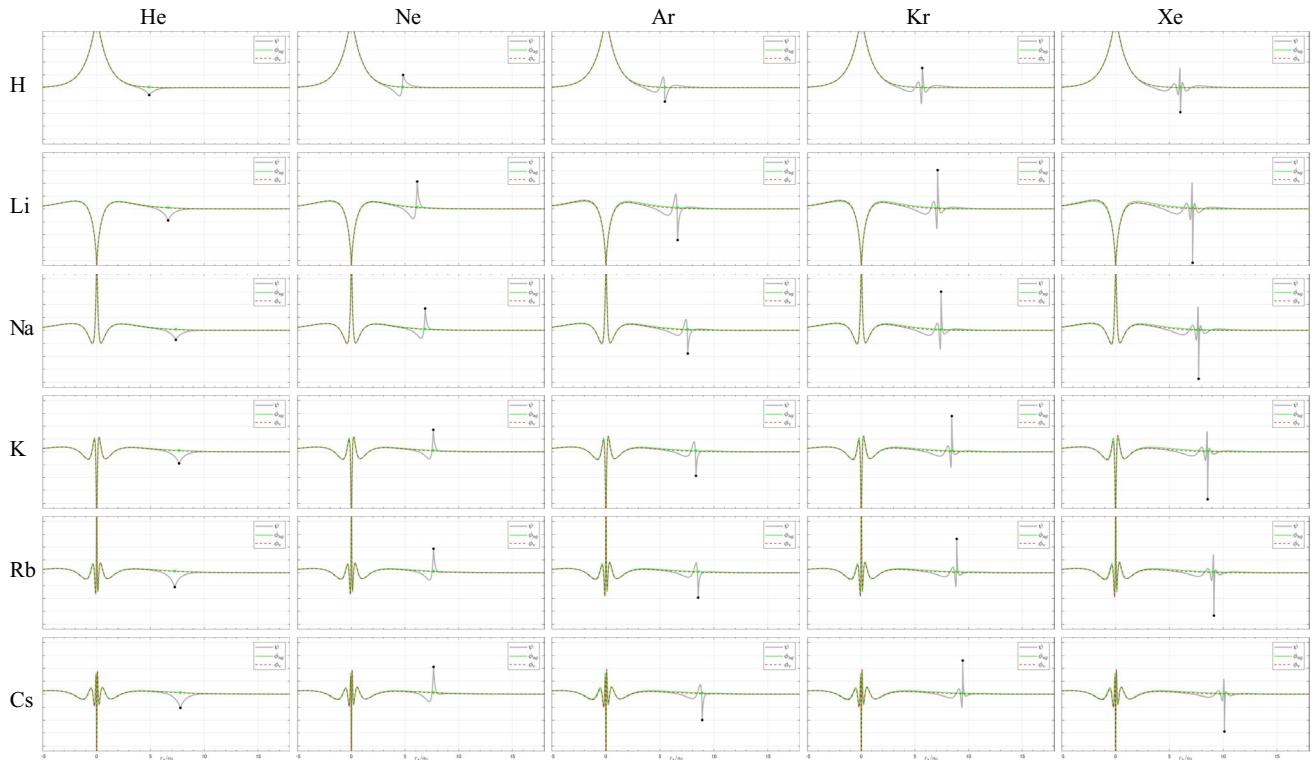

Fig. 4 Wave functions of valence electron for various collision pairs along the internuclear axis. ψ gray solid curve, ϕ_{ag} green solid curve, and ϕ_v red dashed curve. From top to bottom, the collision partners are H, Li, Na, K, Rb, and Cs atoms; from left to right, He, Ne, Ar, Kr, and Xe atoms. The sign of wave function is determined so that the outermost anti-node is positive. These are calculated for the fitting parameter a_h in Fig. 5a using the HFR wave function for ϕ_{ag} of alkali-metal atoms, the CA wave function of the hydrogen atom, and the outermost orbital for the electron density of noble-gas atoms. Due to pseudopotential, $|\phi_v| < |\phi_{ag}|$ at $r_a = R$. The change in electron density due to dispersion force is not included. Each figure is linked to a video (the media file type is MP4). By sliding the seek bar, the enhancement factor and the wave functions are shown at displacements outside the classical turning point R_t, where R_t is from Eq. (21) and Table 2 for 400 K

coefficient c_{oi} mainly comes from the overlap of $\phi_{bi}(\boldsymbol{r}_b)$ with $\phi_{ag}(\boldsymbol{r}_a)$ although the other overlaps with $\phi_{an}(\boldsymbol{r}_a)$ are not negligible. For the He atoms, the p component has been neglected by this OWA [12]. Explicit forms for numerical calculation are given in Appendix C. From Eqs. (10) and (12), the wave function of valence electron is,

$$\psi(\boldsymbol{r}_a, R) = \left\{1 + c_{a2}(R) + c_{o2}(R)\right\}\phi_{ag}(\boldsymbol{r}_a) + \sum_{n>g} c_{ang}(R)\phi_{an}(\boldsymbol{r}_a) - \sum_{i\le g} c_{oi}(R)\phi_{bi}(\boldsymbol{r}_b). \quad (14)$$

For various R, the wave functions $\psi(\boldsymbol{r}_a, R)$, $\phi_v(\boldsymbol{r}_a, R)$, and $\phi_{ag}(\boldsymbol{r}_a)$ at r_a along the internuclear axis are shown in Fig. 4.

3.3.3 Enhancement of electron density at noble-gas nucleus

The wave function of the valence electron at nucleus b presents the magnitude of the spin-exchange interaction between the electron and the noble-gas nucleus. As described in Ref. [13], *the enhancement factor η presents the ratio of the perturbed wave function at the noble-gas nucleus to what it would be in the absence of the noble-gas atom*. In our notation,

$$\psi(\boldsymbol{r}_a = \boldsymbol{R}, R) = \eta\, \phi_{ag}(\boldsymbol{r}_a = \boldsymbol{R}). \quad (15)$$

The enhancement factor, a key parameter for alkali-metal and noble-gas atomic quantum devices [14, 15, 64], is determined by the amplitude of the s orbitals, $\phi_{bi}(\boldsymbol{r}_b = 0)$, where $\boldsymbol{i} = (i, l = 0, m_l = 0, m_S)$. If R is large enough, $\phi_{ag}(\boldsymbol{r}_a)$ is nearly constant as $\phi_{ag}(\boldsymbol{R})$ inside the core of atom b. From Eqs. (13) and (14), the factor $\eta = \left(1 - \sum_i \phi_{bi}(0) \int d^3\boldsymbol{r}_b\, \phi^*_{bi}(\boldsymbol{r}_b)\right)$ is independent of R and determined only by the noble-gas atoms. Therefore, η was assumed to be constant [65]. On the other hand, η decreases as the atoms approach each other. It is because the overlap of $\phi_{ag}(\boldsymbol{r}_a)$ in Eq. (13), which is integrated in three dimensions, becomes smaller and because the mixing coefficients $c_{ang}(R)$ changes to cancel out the dominant part. Therefore, in the region of R where the spin-exchange interaction is effective, the enhancement

factor varies along R differently for each colliding pair. Although $\eta(R)$ decreases, $\eta(R)\phi_{ag}(R)$ increases when atoms are closer to each other. As the temperature increases, the atoms can come even closer to each other, strengthening the spin coupling between valence electrons and noble-gas nuclei [65–68]. If only for the shifts λ, which is the purpose of this work, the non-relativistic HFR wave function can be used to calculate a sufficiently accurate $c_{oi}(R)$. It is because the relativistic correction near $\boldsymbol{r}_b = 0$ is negligible in the integration in Eq. (13). On the other hand, a more precise evaluation of $\eta(R)$ requires the correction at $\boldsymbol{r}_b \approx 0$, which should be significant for heavier noble-gas atoms [69, 70]. The current non-relativistically evaluated enhancement factor and orthogonalized wave function are shown in Fig. 4.

3.4 Statistical average

Hyperfine splitting frequency shifts are calculated by statistical average using perturbation theory with atomic wave functions, pseudopotentials, and dispersion potentials. Owing to a classical turning point, the statistical average reproduces the measured shift over a wide temperature range [8].

3.4.1 Fractional frequency shift

The fractional frequency shift is a relative frequency shift of a function of R, defined by $F(R) = \delta A_g(R)/A_g$ [1, 4]. We assume that the fractional shift consists of two parts, $F(R) = F_{rep}(R) + F_{vdW}(R)$. The first term is due to repulsion force by pseudopotential, as follows,

$$F_{rep}(R) = \left(|\psi(0,R)|^2 - |\phi_{ag}(0)|^2\right) \Big/ |\phi_{ag}(0)|^2. \tag{16}$$

The second-order coefficients are taken within the first-order perturbation theory [8]. Assuming $\phi_{bi}(\boldsymbol{r}_a = 0) = 0$, from Eq. (14),

$$F_{rep}(R) = 2\{c_{a2}(R) + c_{o2}(R)\} + 2\sum_{n>g} c_{ang}(R)\frac{\phi_{an}(0)}{\phi_{ag}(0)} + \left|\sum_{n>g} c_{ang}(R)\frac{\phi_{an}(0)}{\phi_{ag}(0)}\right|^2, \tag{17}$$

where $|\phi_{an}(0)/\phi_{ag}(0)| = \sqrt{A_n/A_g}$ is a correction to the HFR wave functions and A_n is the measured hyperfine constant of ns state of atom a [71–73]. $F_{vdW}(R)$ shows the decrease in the electron density at nucleus a due to dispersion forces. We assume that the negative shift is proportional to the van der Waals potential in Eq. (9) [1],

$$F_{vdW}(R) = V_{vdW}(R)/E_{fit}, \tag{18}$$

where E_{fit} is a parameter for fitting the calculated relative shifts to the measurements.

3.4.2 Classical turning point

For sudden collision of $2\pi\nu_0\tau_c \ll 1$, the ensemble average in Eq. (3) is expressed by a statistical average. The statistical average in the sudden limit (collision duration $\tau_c \to 0$) is of the same form as the static limit (atomic velocity $\to 0$) [26]. For microwave coherence of $h\nu_0 \ll kT$, the density operator $\rho \approx |\psi\rangle(e^{-V/kT}/Z)\langle\psi|$, where k is the Boltzmann constant and the partition function Z is approximately equal to the volume of interest. Therefore, the relative shift in Eq. (1) is [4, 17],

$$\lambda = \int_{R_t}^{\infty} F(R)\, e^{-V(R)/kT} 4\pi R^2 dR. \tag{19}$$

We use the adiabatic potential $V(R)$ in Sect. 3.2.3 and neglect the second-order perturbation energy and the energy increase due to OWA. The classical turning point R_t is the closest distance the colliding pair can approach. The turning point is an indispensable cutoff distance for calculating relative shifts at high temperatures.

In the classical path of each collision, the pair approaches each turning point R_i shown by [4, 22],

$$E_i = V(R_i) + (b_i^2/R_i^2)E_i, \tag{20}$$

where the second term presents the rotational energy at R_i, b_i is the impact parameter, $E_i = mv_i^2/2$, m is the reduced mass, and v_i is the initial relative velocity at $R = \infty$. For the repulsive potentials, $R_i > b_i$. In deep dispersion potentials, the atoms attract each other, and a small R_i is expected; if $V(R_i) < 0$, then $R_i < b_i$. Approximating the ensemble average of Eq. (20) to be decomposed into the respective terms, we define the classical turning point R_t as,

$$V(R_t) = \langle E_i\rangle\left(1 - \left\langle b_i^2/R_i^2\right\rangle\right) = \frac{3}{2}kT(1-\xi), \tag{21}$$

where R_t is greater than the minimum of R_i, $R_t > \min(R_i)$. $\xi = \left\langle b_i^2/R_i^2\right\rangle$ depends on the adiabatic potentials, that is, ξ is larger when the dispersion potential is deeper. Based on the work [8], ξ shown in Table 2 is used.

Since $F(R)$, $V(R)$, and R_t are functions of the fitting parameters, a_h and E_{fit}, the relative shift depends nonlinearly

Table 2 Common parameter ξ in Eq. (21), used in Fig. 5a–f

	He	Ne	Ar	Kr	Xe
H	0.60	0.63	0.67	0.70	0.73
Li	0.63	0.67	0.70	0.73	0.77
Na	0.67	0.70	0.73	0.77	0.80
K	0.70	0.73	0.77	0.80	0.83
Rb	0.73	0.77	0.80	0.83	0.87
Cs	0.77	0.80	0.83	0.87	0.90

on the parameters and is obtained by numerical calculation. The overlap integrals in Eqs. (11) and (13) are independent of the fitting parameters. Therefore, the fitting procedure is not time-consuming once the overlaps are calculated.

4 Discussion

The measured relative shifts were fitted by two parameters, $E_{\rm fit}^{-1}$ and $a_{\rm h}$, as shown in Fig. 1. At a temperature, the calculated shift increases as $a_{\rm h}$ increases, and the increase in shift is canceled out by the increases in $E_{\rm fit}^{-1}$, indicating a positive correlation between these parameters. Nevertheless, fitting over a wide temperature range provides unique parameters definitively. Since the calculated shift is the offset of the respective large shifts due to $E_{\rm fit}^{-1}$ and $a_{\rm h}$, the measured shift gives information on the small changes in the two parameters. As shown in the comparison of the fitting curves using the HFR wave function and the CA wave function for the ground state, it is possible to fit the calculations to the measured shifts using either wave function. Furthermore, fitting is possible for any electron density distribution of noble-gas atoms, whether OMT, ALC, or DLT. Nevertheless, the parameters obtained are different, as shown in Fig. 5a–f, where $E_{\rm fit}^{-1}$ is normalized by $E_{\rm c}^{-1}$ [8]. The characteristic energy $E_{\rm c}$, obtained from the mean excitation energies of atoms a and b, mainly normalizes the properties of the atom a [1, 6]. In the following, we examine which combination reasonably explains the measurements.

Figure 5f obtained by CA, DLT, and OWA with fitting parameters $E_{\rm fit}^{-1}$ and $a_{\rm h}$, can be compared with Fig. 9a in Ref. [8], which was obtained by CA, DLT, and no OWA with fitting parameters $E_{\rm fit}^{-1}$ and ξ. The difference in these parameter maps is mainly due to the use of OWA or not. Therefore, OWA is essential for calculating the electron density at the nucleus a. The vertical parameter $a_{\rm h}$ is smaller by the DLT, ALS, and OMT distributions in that order because a wider distribution of core electrons better reproduces the foot of the adiabatic potential. For the same reason, in the case of hydrogen, reasonable values of $a_{\rm h}$ are obtained by OMT in each noble gas. In Fig. 5e, f, too high pseudopotentials of delta function imply the large radii of the hard spheres, some of which are larger than the respective classical turning points shown in Fig. 4. Therefore, the fitting result by DLT does not correspond well with scattering theory. The repulsion potentials were calculated based on the CA wave function [52], but as the alkali-metal atoms become heavier, the CA wave function differs from the HFR wave function. In addition, the parameter $a_{\rm h}$ is smaller for the HFR wave function than for the CA wave function. In Fig. 5a, $a_{\rm h}$ becomes less alkali-metal dependent for each noble-gas atom, where the measured hyperfine splitting frequencies are fitted based on the HFR wave function. Therefore, the fitting by the HFR wave function and the OMT electron-density distribution is the best and physically reasonable. Tables 3 and 4 show the fitting parameters.

Table 3 Fitting parameter $a_{\rm h}$ obtained in Fig. 5a, in Bohr radii

	He	Ne	Ar	Kr	Xe
H	4.308	4.911	8.288	8.443	8.615
Li	1.533	1.344	3.286	4.669	5.539
Na	1.964	1.654	4.135	4.428	5.631
K	1.241	1.499	3.704	4.566	5.807
Rb	0.844	1.275	3.412	4.531	5.937
Cs	0.810	1.034	2.998	4.084	5.824

Table 4 Fitting parameter $E_{\rm fit}^{-1}$ in Fig. 5a, in units of hartree^{-1}

	He	Ne	Ar	Kr	Xe
H	13.10	10.30	9.20	9.00	9.40
Li	9.80	12.70	15.50	17.00	15.90
Na	16.20	16.80	19.80	18.60	18.30
K	10.50	20.10	23.00	24.50	23.00
Rb	6.80	17.70	23.20	25.50	25.50
Cs	6.80	18.00	26.30	31.30	33.50

In Refs. [7, 8], $a_{\rm h}$ was normalized by the electric-dipole polarizability α and van der Waals radius $R_{\rm vdw}$. See Table 1. Although it appeared to be successful, it was not the only solution. That is, α can be replaced by the number of core electrons $N_{\rm e}$, and $R_{\rm vdw}$ is macroscopic rather than an atomic parameter. To find a more effective normalization, the atomic radius $R_{\rm hfr}$ is applied to Fig. 5a, resulting in the parameter map shown in Fig. 6. The obtained parameters are close to each other for all combinations of alkali-metal and noble-gas atoms and, due to unknown reasons, lie near a straight line. Once the reason for the linear relationship is clarified, this relationship can be used to reduce the number of fitting parameters. At present, neglecting the linear relation, the center of gravity is at $a_{\rm h}/R_{\rm hfr} = 2.58 \pm 0.53$ and $E_{\rm c}/E_{\rm fit} = 1.00 \pm 0.30$. Normalization by $E_{\rm c}$ happens to work, judging from the presence of various energies $E_{\rm c}$ [6] and dispersion potentials [7]. According to the scattering theory, the height of the pseudopotential after deconvolution in Eq. (6) represents the radius of the hard-sphere model, which is consistent with and less than the turning point, $a_{\rm h} < R_t$. At the high-temperature approximation, in collisions with an atom with a single valence electron, the effective radius of the sphere of noble gas atoms can be taken as $2.6R_{\rm hfr}$. Our model self-consistently simulates collision-induced resonance shifts even when the noble-gas atom is of a larger radius than the paramagnetic atoms and cannot be approximated by a delta function.

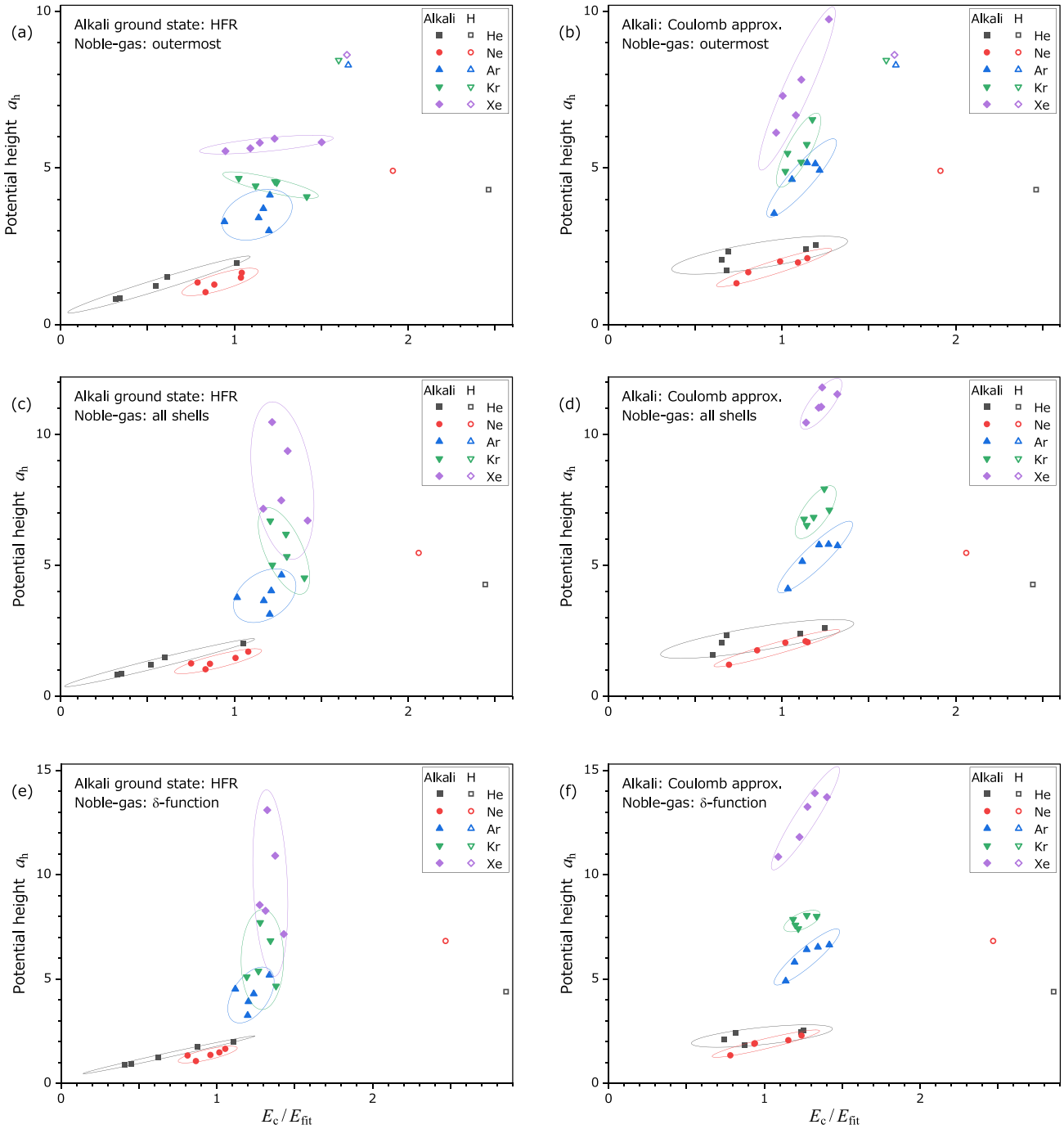

Fig. 5 Fitting parameters by using Coulomb-approximation (CA) and Hartree-Fock-Roothaan (HFR) wave functions. Electron densities of noble-gas atoms are assumed to be delta function (DLT), all core orbitals (ALC), and outermost core orbitals (OMT). **a** HFR and OMT, **b** CA and OMT, **c** HFR and ALC, **d** CA and ALC, **e** HFR and DLT, **f** CA and DLT. For hydrogen (open marks), the CA wave function is used for the ground state of the valence electron in all the maps. For the pairs H-Ar, H-Kr, and H-Xe, the parameter a_h is too large and out of range in **c**, **d**, **e**, and **f**. Each elliptical region, a guide for the eye, contains the closed marks for alkali-metal atoms

5 Summary

A perturbation theory for the collisional shifts of hyperfine resonances was presented that accounted for the finite size of both colliding atoms by the modified pseudopotentials. The orthogonalized wave approximation was essential for calculating the electron density at the position of the paramagnetic atoms. With external resources such as the theoretical dispersion potentials and the characteristic energies, the collisional shifts of hydrogen and alkali-metal

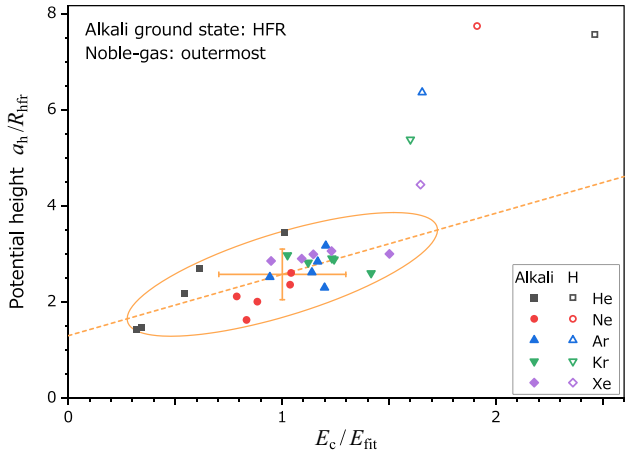

Fig. 6 Fitting parameters by the HFR wave function for the alkali-metal ground state and the electron density of the outermost orbital for noble-gas atoms. The CA wave function is used for hydrogen. The vertical axis shows the potential height normalized by atomic radius. The elliptical region, a guide for the eye, contains the closed marks for alkali-metal atoms. The dashed line shows fitting, $a_h/R_{hfr} = (1.30 \pm 0.27) + (1.27 \pm 0.26)E_c/E_{fit}$. The error bars indicate the center of gravity of the parameters for alkali-metal atoms

atoms in noble gases were calculated numerically and fitted to the measurements. The calculations were compared using the Coulomb-approximation wave function and the Hartree-Fock-Roothaan wave function for paramagnetic atoms and using various electron distributions for noble gas atoms. As a result, the best fits were obtained by the Hartree–Fock–Roothaan wave function for the ground state of paramagnetic atoms and the outermost occupied orbitals for the electron density of the noble gas atoms. The fitting parameters, $a_h/R_{hfr} = 2.6$ and $E_c/E_{fit} = 1.0$, were obtained for all combinations of alkali-metal atoms and noble-gas atoms. The linear relation between fitting parameters was found but remains to be addressed in future studies.

A. Expectation value of interaction Hamiltonian

The expectation value of the interaction Hamiltonian is obtained in Eq. (7). This is the convolution of $|\phi_{ag}(\boldsymbol{r}_a)|^2 = R^2_{ag}(r_a)/4\pi$ and $\rho_b(\boldsymbol{r}_b) = R^2_{b\rho}(r_b)/4\pi$. Using $d^3\boldsymbol{r}_a = 2\pi r_a^2 \sin\theta_a dr_a d\theta_a$, the expectation value is

$$V_g(\boldsymbol{R}) = \frac{V_h}{2}\int_0^\infty dr_a \int_0^\pi d\theta_a\, r_a^2 \sin\theta_a\, R^2_{ag}(r_a)\, R^2_{b\rho}(r_b). \quad (22)$$

where $r_b^2 = R^2 + r_a^2 - 2Rr_a\cos\theta_a$. This convolution can be calculated as

$$V_g(\boldsymbol{R}) = \frac{V_h}{2}\int_0^\infty dr_b \int_0^\pi d\theta_b\, r_b^2 \sin\theta_b\, R^2_{ag}(r_a)\, R^2_{b\rho}(r_b), \quad (23)$$

where $r_a^2 = R^2 + r_b^2 + 2Rr_b\cos\theta_b$. Equation (23) is useful when the spatial extent of $R_{b\rho}(r_b)$ is smaller than $R_{ag}(r_a)$. The convolution of the shifted function can be altered by forward and inverse Fourier transforms. The Fourier transform is generally faster than the convolution itself. Nevertheless, the above convolution requires only a narrow integration domain by utilizing the spherical symmetry of the core orbitals and the finite size of the wave function, while the Fourier transform needs to be performed over a wide range. Therefore, the above convolutions are calculated faster than the Fourier transform.

B. Convolution of valence electron wave functions and noble-gas electron density

In Eq. (11), $\phi_{ag}(\boldsymbol{r}_a)$ and $\rho_b(\boldsymbol{r}_b)$ are independent of the azimuthal angle φ. From $\int_0^{2\pi} Y_{\ell m_\ell \neq 0}(\theta,\varphi)d\varphi = 0$, only the part of the wave function $\phi^*_{an}(\boldsymbol{r}_a), C^{jm}_{l0\frac{1}{2}m} R_{an}(r_a) Y_{\ell 0}(\theta_a, 0)$, gives a non-zero integral value, where $\boldsymbol{n} = (n,l,j,m)$ and $C^{jm}_{l0\frac{1}{2}m} = (-1)^{(j-l-\frac{1}{2})(m+\frac{1}{2})}\sqrt{\frac{j+1/2}{2l+1}}$. Therefore, the first-order coefficient of pseudopotential perturbation is,

$$c_{a\boldsymbol{ng}}(R) = -\frac{V_h}{E_n} C^{jm}_{l0\frac{1}{2}m}\int_0^\infty dr_a \int_0^\pi d\theta_a\, r_a^2 \sin\theta_a \times \sqrt{\pi}\, Y_{\ell 0}(\theta_a, 0) R_{a\boldsymbol{n}}(r_a) R_{ag}(r_a) R^2_{b\rho}(r_b). \quad (24)$$

In spherical coordinate centered at nucleus b,

$$c_{a\boldsymbol{ng}}(R) = -\frac{V_h}{E_n} C^{jm}_{l0\frac{1}{2}m}\int_0^\infty dr_b \int_0^\pi d\theta_b\, r_b^2 \sin\theta_b \times \sqrt{\pi}\, Y_{\ell 0}(\theta_a, 0) R_{a\boldsymbol{n}}(r_a) R_{ag}(r_a) R^2_{b\rho}(r_b), \quad (25)$$

where $r_a\cos\theta_a = R + r_b\cos\theta_b$ is used in $Y_{\ell 0}(\theta_a, 0)$.

C. Overlap of valence electron orbital and noble-gas core orbitals

The uncoupled wave function, $\phi^*_{b\boldsymbol{i}}(\boldsymbol{r}_b) = R_{b\boldsymbol{i}}(r_b) Y^*_{l_b m_l}(\theta_b, \varphi_b)\chi_{m_S}(\sigma_b)$, is considered for atom b. As shown in Appendix B, m_j of the mixing state is the same as m_S of the ground state. Let $m_S = 1/2$ and consider the excited states of $m_j = 1/2$ for atom a. The s state of $l_a = 0$ is,

$$\phi_{a\boldsymbol{n}}(\boldsymbol{r}_a) = R_{an0\frac{1}{2}}(r_a) Y_{00}(\theta_a, \varphi_a)\chi_{\frac{1}{2}}(\sigma_a). \quad (26)$$

The state of $l_a > 0$ is,

$$\begin{aligned}\phi_{a\boldsymbol{n}}(\boldsymbol{r}_a) &= R_{anlj}(r_a)\sum_{m_l,m_S} C^{j\frac{1}{2}}_{lm_l\frac{1}{2}\sigma} Y_{lm_l}(\theta_a,\varphi_a)\chi_{m_S}(\sigma_a)\\ &= \left(C^{j\frac{1}{2}}_{l0\frac{1}{2}\frac{1}{2}} Y_{l0}(\theta_a,\varphi_a) + C^{j\frac{1}{2}}_{l1\frac{1}{2}-\frac{1}{2}} Y_{l1}(\theta_a,\varphi_a)\right)R_{anlj}(r_a).\end{aligned} \tag{27}$$

For $l_a = 0$, the term giving a non-zero integral value in Eq. (13) is,

$$\begin{aligned}\phi^*_{b\boldsymbol{i}}(\boldsymbol{r}_b)\phi_{a\boldsymbol{n}}(\boldsymbol{r}_a) &= R_{bil_b}(r_b)Y^*_{l_b0}(\theta_b,\varphi_b)Y_{00}(\theta_a,\varphi_a)R_{an0\frac{1}{2}}(r_a)\\ &= \frac{\sqrt{2l_b+1}}{4\pi}P_{l_b}(\cos\theta_b)R_{bil_b}(r_b)R_{an0\frac{1}{2}}(r_a).\end{aligned} \tag{28}$$

For $l_b = 0$,

$$\begin{aligned}\phi^*_{b\boldsymbol{i}}(\boldsymbol{r}_b)\phi_{a\boldsymbol{n}}(\boldsymbol{r}_a) &= R_{bi0}(r_b)Y^*_{00}(\theta_b,\varphi_b)C^{j\frac{1}{2}}_{l0\frac{1}{2}\frac{1}{2}}Y_{l0}(\theta_a,\varphi_a)R_{anlj}(r_a)\\ &= \pm\frac{\sqrt{j_a+\frac{1}{2}}}{4\pi}P_{l_a}(\cos\theta_a)R_{bi0}(r_b)R_{anlj}(r_a),\end{aligned} \tag{29}$$

where the double sign in the last line is in the same order as $j_a = l_a \pm 1/2$. For $l_a l_b \neq 0$ and $m_{l_b} = 0$,

$$\begin{aligned}\phi^*_{b\boldsymbol{i}}(\boldsymbol{r}_b)\phi_{a\boldsymbol{n}}(\boldsymbol{r}_a) &= R_{bil_b}(r_b)Y^*_{l_b0}(\theta_b,\varphi_b)\\ &\times\left(C^{j\frac{1}{2}}_{l0\frac{1}{2}\frac{1}{2}}Y_{l0}(\theta_a,\varphi_a) + C^{j\frac{1}{2}}_{l1\frac{1}{2}-\frac{1}{2}}Y_{l1}(\theta_a,\varphi_a)\right)R_{anlj}(r_a).\end{aligned} \tag{30}$$

Since the second term is zeroed by integration, only the first term is considered, as follows,

$$\begin{aligned}&R_{bil_b}(r_b)Y^*_{l_b0}(\theta_b,\varphi_b)C^{j_a\frac{1}{2}}_{l_a0\frac{1}{2}\frac{1}{2}}Y_{l_a0}(\theta_a,\varphi_a)R_{anl_aj_a}(r_a)\\ &= \pm\frac{\sqrt{(2l_b+1)(j_a+\frac{1}{2})}}{4\pi}P_{l_b}(\cos\theta_b)P_{l_a}(\cos\theta_a)R_{bil_b}(r_b)R_{anl_aj_a}(r_a).\end{aligned} \tag{31}$$

For $l_a l_b \neq 0$ and $m_{l_b} \neq 0$, the term with $m_{l_b} = 1$ remains as,

$$\begin{aligned}\phi^*_{b\boldsymbol{i}}(\boldsymbol{r}_b)\phi_{a\boldsymbol{n}}(\boldsymbol{r}_a) &= R_{bil_b}(r_b)Y^*_{l_b1}(\theta_b,\varphi_b)\\ &\times\left(C^{j\frac{1}{2}}_{l0\frac{1}{2}\frac{1}{2}}Y_{l0}(\theta_a,\varphi_a) + C^{j\frac{1}{2}}_{l1\frac{1}{2}-\frac{1}{2}}Y_{l1}(\theta_a,\varphi_a)\right)R_{anlj}(r_a).\end{aligned} \tag{32}$$

Here, only the second term is considered,

$$\begin{aligned}&R_{bil_b}(r_b)Y^*_{l_b1}(\theta_b,\varphi_b)C^{j\frac{1}{2}}_{l1\frac{1}{2}-\frac{1}{2}}Y_{l1}(\theta_a,\varphi_a)R_{anlj}(r_a)\\ &= \frac{\sqrt{(2l_b+1)(l_a+\frac{1}{2}\mp\frac{1}{2})(l_a-1)!(l_b-1)!}}{4\pi\sqrt{(l_a+1)!(l_b+1)!}}\\ &\times P^1_{l_b}(\cos\theta_b)P^1_{l_a}(\cos\theta_a)R_{bil_b}(r_b)R_{anlj}(r_a).\end{aligned} \tag{33}$$

The sum extends over $(n, l_a, j, 1/2)$ for each $(i, l_b, m_{l_b}, 1/2)$ in Eq. (13).

Supplementary Information The online version contains supplementary material available at https://doi.org/10.1007/s00340-024-08203-2.

Acknowledgements This study was funded by JSPS (Grant No. 23H01845).

Data availability The data that support the findings of this study are available from the corresponding author upon reasonable request.

References

1. J. Vanier, C. Audoin, *The Quantum Physics of Atomic Frequency Standards* (Hilger, Bristol, 1989)
2. J. Camparo, The rubidium atomic clock and basic research. Phys. Today **60**(11), 33–39 (2007)
3. S. Ray, G. Das, P. Maldonado, and Arnold C. Wahl. Theoretical evaluation of the fractional hyperfine pressure shift of paramagnetic atoms in a noble gas. *Phys. Rev. A* **2**, 2196–2200 (1970)
4. P.J. Oreto, Y.-Y. Jau, A.B. Post, N.N. Kuzma, W. Happer, Buffer-gas-induced shift and broadening of hyperfine resonances in alkali-metal vapors. Phys. Rev. A **69**, 042716 (2004)
5. J.C. Camparo, Semiempirical theory of Carver rates in alkali/noble-gas systems. J. Chem. Phys. **126**(24), 244310 (2007)
6. B.H. McGuyer, Hyperfine-frequency shifts of alkali-metal atoms during long-range collisions. Phys. Rev. A **87**, 054702 (2013)
7. K. Ishikawa, Pseudopotential analysis on hyperfine splitting frequency shift of alkali-metal atoms in noble gases, revisited. J. Chem. Phys. **158**(8), 084306 (2023)
8. K. Ishikawa, Flying characterization of colliding partners by hyperfine splitting frequency of neutral paramagnetic atoms. J. Chem. Phys. **159**(6), 064303 (2023)
9. D. R. Bates, A. Damgaard, H. S. W. Massey. The calculation of the absolute strengths of spectral lines. *Philos. Trans. R. Soc. Lond. Ser. A* **242**(842), 101 (1949)
10. E. Clementi, C. Roetti, Roothaan–Hartree–Fock atomic wavefunctions: basis functions and their coefficients for ground and certain excited states of neutral and ionized atoms, $Z \leq 54$. At. Data Nucl. Data Tables **14**(3), 177 (1974)
11. A.D. McLean, R.S. McLean, Roothaan–Hartree–Fock atomic wave functions Slater basis-set expansions for Z = 55–92. At. Data Nucl. Data Tables **26**(3), 197–381 (1981)
12. T.G. Walker, K. Bonin, W. Happer, Electron-noble-gas spin-flip scattering at low energy. Phys. Rev. A **35**, 3749–3752 (1987)
13. T.G. Walker, W. Happer, Spin-exchange optical pumping of noble-gas nuclei. Rev. Mod. Phys. **69**, 629 (1997)
14. K. Wei, T. Zhao, X. Fang, Z. Xu, C. Liu, Q. Cao, A. Wickenbrock, Y. Hu, W. Ji, J. Fang, D. Budker, Ultrasensitive atomic comagnetometer with enhanced nuclear spin coherence. Phys. Rev. Lett. **130**, 063201 (2023)
15. J. Lee, M. Lisanti, W.A. Terrano, M. Romalis, Laboratory constraints on the neutron-spin coupling of feV-scale axions. Phys. Rev. X **13**, 011050 (2023)
16. D.K. Walter, W. Happer, T.G. Walker, Estimates of the relative magnitudes of the isotropic and anisotropic magnetic-dipole hyperfine interactions in alkali-metal-noble-gas systems. Phys. Rev. A **58**, 3642–3653 (1998)

17. B. L. Bean and R. H. Lambert. Temperature dependence of hyperfine density shifts. III. ^{23}Na, ^{39}K, and ^{85}Rb in He, Ne, Ar, and N_2. *Phys. Rev. A* **12**, 1498–1502 (1975)
18. F. Gong, Y.-Y. Jau, W. Happer, Nonlinear pressure shifts of alkali-metal atoms in inert gases. Phys. Rev. Lett. **100**, 233002 (2008)
19. B.H. McGuyer, Isotope study of the nonlinear pressure shifts of ^{85}Rb and ^{87}Rb hyperfine resonances in Ar, Kr, and Xe buffer gases. J. Chem. Phys. **158**(14), 144304 (2023)
20. A. Laskowski, N.P. Mehta, Homonuclear ultracold elastic *s*-wave collisions of alkali-metal atoms via multichannel quantum defect theory. Phys. Rev. A **108**, 043306 (2023)
21. A. Tsinovoy, O. Katz, A. Landau, N. Moiseyev, Enhanced coupling of electron and nuclear spins by quantum tunneling resonances. Phys. Rev. Lett. **128**, 013401 (2022)
22. W. Happer, Y.-Y. Jau, T.G. Walker, *Optically Pumped Atoms* (Wiley-VCH, Weinheim, 2010)
23. K. Ishikawa, M. Yamamoto, Ground-state decoherence of lithium atoms by diatomic polar molecules and noble-gas atoms. Appl. Phys. B **129**(7), 113 (2023)
24. R. Shaham, O. Katz, O. Firstenberg, Quantum dynamics of collective spin states in a thermal gas. Phys. Rev. A **102**, 012822 (2020)
25. D. Manzano, A short introduction to the Lindblad master equation. AIP Adv. **10**(2), 025106 (2020)
26. N. Allard, J. Kielkopf, The effect of neutral nonresonant collisions on atomic spectral lines. Rev. Mod. Phys. **54**, 1103–1182 (1982)
27. J. J. Wright, L. C. Balling, and R. H. Lambert. Temperature dependence of hyperfine pressure shifts. I. Deuterium in Helium from -135 to 400 °C. *Phys. Rev. A* **1**, 1018–1021 (1970)
28. L. Wilmer Anderson, Francis M. Pipkin, and James C. Baird. Hyperfine structure of hydrogen, deuterium, and tritium, Errata1, Errata2. *Phys. Rev.* **120**, 1279–1289 (1960)
29. F.M. Pipkin, R.H. Lambert, Hyperfine Splittings of Hydrogen and Tritium. II. Phys. Rev. **127**, 787–792 (1962)
30. R.A. Brown, F.M. Pipkin, Pressure shifts of hyperfine splitting of hydrogen and tritium in argon. Phys. Rev. **174**, 48–56 (1968)
31. E. S. Ensberg and C. L. Morgan, in *Precision Measurement and Fundamental Constants, National Bureau of Standards Special Publication*, vol 343, ed. by D. N. Langenberg and B. N. Taylor (National Bureau of Standards (U.S.), 1971), pp 321–325
32. J.J. Wright, L.C. Balling, R.H. Lambert, Hyperfine splittings and pressure shifts of Li^6 and Li^7. Phys. Rev. **183**, 180 (1969)
33. Kiyoshi Ishikawa, Noble-gas atoms characterized by hyperfine frequency shift of lithium atom. J. Chem. Phys. **156**(14), 144301 (2022)
34. A. T. Ramsey, L. Wilmer Anderson. Pressure shifts in the ^{23}Na hyperfine frequency. *J. Chem. Phys.*, **43**(1), 191–194 (1965)
35. B. L. Bean and R. H. Lambert. Temperature dependence of hyperfine density shifts. IV. ^{23}Na, ^{39}K, and ^{85}Rb in He, Ne, Ar, and N_2 at low temperatures. *Phys. Rev. A* **13**, 492–494 (1976)
36. Arnold L. Bloom, John B. Carr, Pressure shifts in the hyperfine structure constant of potassium. Phys. Rev. **119**, 1946–1947 (1960)
37. B.H. McGuyer, T. Xia, Y.-Y. Jau, W. Happer, Hyperfine frequencies of ^{87}Rb and ^{133}Cs atoms in Xe gas. Phys. Rev. A **84**, 030501 (2011)
38. P.L. Bender, E.C. Beaty, A.R. Chi, Optical detection of narrow Rb ^{87} hyperfine absorption lines. Phys. Rev. Lett. **1**, 311–313 (1958)
39. J. Vanier, J.-F. Simard, J.-S. Boulanger. Relaxation and frequency shifts in the ground state of Rb^{85}. *Phys. Rev. A* **9**, 1031–1040 (1974)
40. V.V. Batygin, V.S. Zholnerov, Temperature dependence of the hyperfine transition frequency of the ground state of Rb^{87} in a buffer medium. Opt. Spectrosc. (USSR) **39**(3), 254–255 (1975)
41. L.-C. Ha, X. Zhang, N. Dao, K. Richard Overstreet. D_1 line broadening and hyperfine frequency shift coefficients for ^{87}Rb and ^{133}Cs in Ne, Ar, and N_2. *Phys. Rev. A* **103**, 022826 (2021)
42. Gilles Missout, Jacques Vanier, Pressure and temperature coefficients of the more commonly used buffer gases in rubidium vapor frequency standards. IEEE Trans. Instrum. Meas. **24**(2), 180–184 (1975)
43. E. S. Ensberg, G. zu Putlitz. Nonlinear hyperfine pressure shift by optical pumping with white light. *Phys. Rev. Lett.* **22**, 1349–1351 (1969)
44. J. Vanier, R. Kunski, N. Cyr, J.Y. Savard, M. Tetu, On hyperfine frequency shifts caused by buffer gases: application to the optically pumped passive rubidium frequency standard. J. Appl. Phys. **53**(8), 5387–5391 (1982)
45. M. Arditi, T.R. Carver, Pressure, light, and temperature shifts in optical detection of 0–0 hyperfine resonance of alkali metals. Phys. Rev. **124**, 800–809 (1961)
46. E.C. Beaty, P.L. Bender, A.R. Chi, Narrow hyperfine absorption lines of Cs ^{133} in various buffer gases. Phys. Rev. **112**, 450–451 (1958)
47. F. Strumia, N. Beverini, A. Moretti, G. Rovera. Optimization of the buffer gas mixture for optically pumped Cs frequency standards. *30th Annual Sympos. Freq. Control*, pp 468–472 (1976)
48. C.W. Beer, R.A. Bernheim, Hyperfine pressure shift of ^{133}Cs atoms in noble and molecular buffer gases. Phys. Rev. A **13**, 1052–1057 (1976)
49. M. Arditi, T.R. Carver, Frequency shift of the zero-field hyperfine splitting of Cs ^{133} produced by various buffer gases. Phys. Rev. **112**, 449–449 (1958)
50. Olga Kozlova, Stéphane. Guérandel, Emeric de Clercq, Temperature and pressure shift of the Cs clock transition in the presence of buffer gases: Ne, N_2. Ar. Phys. Rev. A **83**, 062714 (2011)
51. E.U. Condon, G. Shortley, *The Theory of Atomic Spectra* (Cambridge University Press, Cambridge, 1935)
52. S.H. Patil, Adiabatic potentials for alkali-inert gas systems in the ground state. J. Chem. Phys. **94**(12), 8089 (1991)
53. E. Fermi, Sopra lo Spostamento per Pressione delle Righe Elevate delle Serie Spettrali. Nuovo Cimento **11**, 157 (1934)
54. U. Asaf, K. Rupnik, G. Reisfeld, S.P. McGlynn, Pressure shifts and electron scattering lengths in atomic and molecular gases. J. Chem. Phys. **99**(4), 2560–2566 (1993)
55. N. Thaicharoen, R. Cardman, G. Raithel. Rydberg-EIT of ^{85}Rb vapor in a cell with Ne buffer gas. *arXiv, physics.atom-ph*, pp. 2308.07554 (2023)
56. G. Reisfeld, U. Asaf, Relation between the electron scattering length and the van der Waals approximation to the equation of state. Phys. Rev. A **49**, 348 (1994)
57. U. Hohm, K. Kerl, Interferometric measurements of the dipole polarizability α of molecules between 300 K and 1100 K. Mol. Phys. **69**(5), 803–817 (1990)
58. T.F. O'Malley, Extrapolation of electron-rare gas atom cross sections to zero energy. Phys. Rev. **130**, 1020 (1963)
59. E. Clementi, D. L. Raimondi, W. P. Reinhardt. Atomic screening constants from SCF functions. II. Atoms with 37 to 86 electrons. *J. Chem. Phys.* **47**(4), 1300–1307 (1967)
60. K.T. Tang, J.P. Toennies, A combining rule calculation of the van der Waals potentials of the rare-gas hydrides. Chem. Phys. **156**(3), 413–425 (1991)
61. S.J. Buckman, C.W. Clark, Atomic negative-ion resonances. Rev. Mod. Phys. **66**, 539–655 (1994)
62. NIST. Atomic Spectra Database. *NIST Standard Reference Database* (2023)

63. M. Horbatsch, E.A. Hessels, Tabulation of the bound-state energies of atomic hydrogen. Phys. Rev. A **93**, 022513 (2016)
64. A.B. Baranga, S. Appelt, M.V. Romalis, C.J. Erickson, A.R. Young, G.D. Cates, W. Happer, Polarization of ^{3}He by spin exchange with optically pumped Rb and K vapors. Phys. Rev. Lett. **80**, 2801–2804 (1998)
65. S. R. Schaefer, G. D. Cates, T.-R. Chien, D. Gonatas, W. Happer, T. G. Walker. Frequency shifts of the magnetic-resonance spectrum of mixtures of nuclear spin-polarized noble gases and vapors of spin-polarized alkali-metal atoms. *Phys. Rev. A* **39**, 5613–5623 (1989)
66. T.G. Walker, Estimates of spin-exchange parameters for alkali-metal-noble-gas pairs. Phys. Rev. A **40**, 4959–4964 (1989)
67. M. V. Romalis. Laser polarized 3He target used for a precision measurement of the neutron spin structure. *PhD thesis, Princeton University* (1997)
68. E. Babcock, I.A. Nelson, S. Kadlecek, T.G. Walker, ^{3} He polarization-dependent EPR frequency shifts of alkali-metal-^{3} He pairs. Phys. Rev. A **71**, 013414 (2005)
69. I.P. Grant, Relativistic calculation of atomic structures. Adv. Phys. **19**(82), 747–811 (1970)
70. Y.-K. Kim, Relativistic self-consistent-field theory for closed-shell atoms. Phys. Rev. **154**, 17–39 (1967)
71. E. Arimondo, M. Inguscio, P. Violino, Experimental determinations of the hyperfine structure in the alkali atoms. Rev. Mod. Phys. **49**, 31–75 (1977)
72. M. Allegrini, E. Arimondo, L.A. Orozco, Survey of hyperfine structure measurements in alkali atoms. J. Phys. Chem. Ref. Data **51**(4), 043102 (2022)
73. R.G. Bullis, C. Rasor, W.L. Tavis, S.A. Johnson, M.R. Weiss, D.C. Yost, Ramsey spectroscopy of the $2S_{1/2}$ hyperfine interval in atomic hydrogen. Phys. Rev. Lett. **130**, 203001 (2023)